

Disk Wind Feedback from High-mass Protostars. V. Application of Multi-Modal Machine Learning to Characterize Outflow Properties

DUO XU,^{1,2} IOANA A. STELEA,^{3,4} JOSHUA S. SPEAGLE (沈佳士),^{5,6,7,8} YICHEN ZHANG,⁹ AND JONATHAN C. TAN^{10,11}

¹Canadian Institute for Theoretical Astrophysics, University of Toronto, 60 St. George Street, Toronto, ON M5S 3H8, Canada

²Department of Astronomy, University of Virginia, Charlottesville, VA 22904-4235, USA

³Department of Astronomy, Columbia University, New York, NY 10027, USA

⁴Department of Astronomy, University of Wisconsin-Madison, Madison, WI 53706-1507, USA

⁵Department of Statistical Sciences, University of Toronto, 9th Floor, Ontario Power Building, 700 University Ave, Toronto, ON M5G 1Z5, Canada

⁶David A. Dunlap Department of Astronomy & Astrophysics, University of Toronto, 50 St. George Street, Toronto, ON M5S 3H4, Canada

⁷Dunlap Institute for Astronomy & Astrophysics, University of Toronto, 50 St. George Street, Toronto, ON M5S 3H4, Canada

⁸Data Sciences Institute, University of Toronto, 17th Floor, Ontario Power Building, 700 University Ave, Toronto, ON M5G 1Z5, Canada

⁹Department of Astronomy, Shanghai Jiao Tong University, 800 Dongchuan Rd., Minhang, Shanghai 200240, China

¹⁰Department of Astronomy and Virginia Institute for Theoretical Astronomy (VITA), University of Virginia, Charlottesville, VA 22904-4235, USA

¹¹Department of Physics & Astronomy, Chalmers University of Technology, SE-412 96 Gothenburg, Sweden

ABSTRACT

Characterizing protostellar outflows is fundamental to understanding star formation feedback, yet traditional methods are often hindered by projection effects and complex morphologies. We present a multi-modal deep learning framework that jointly leverages spatial and spectral information from CO observations to infer outflow mass, inclination, and position angle (*PA*). Our model, trained on synthetic ALMA observations generated from 3D magnetohydrodynamic simulations, utilizes a cross-attention fusion mechanism to integrate morphological and kinematic features with probabilistic uncertainty estimation. Our results demonstrate that Vision Transformer architectures significantly outperform convolutional networks, showing remarkable robustness to reduced spatial resolution. Interpretability analysis reveals a physically consistent hierarchy: spatial features dominate across all parameters, whereas spectral profiles provide secondary constraints for mass and inclination. Applied to observational ALMA data, the framework delivers stable mass and *PA* estimates with exceptionally tightly constrained inclination angles. This study establishes multi-modal deep learning as a powerful, interpretable tool for overcoming projection biases in high-mass star formation studies.

Keywords: Interstellar medium (847) — Molecular clouds (1072) — Radiative transfer (1335) — Stellar jets (1607) — Stellar winds (1636) — Convolutional neural networks (1938) — Magnetohydrodynamics (1964)

1. INTRODUCTION

The formation of stars from the gravitational collapse of dense molecular clouds is a fundamental process that drives the evolution of galaxies and provides foundations for planetary systems. During the earliest stages of protostellar evolution, young stars launch bipolar protostellar outflows that play a crucial role in removing angular

momentum from the accretion disk, regulating the inflow of material, and injecting mass, momentum, and energy into the surrounding interstellar medium (e.g., M. Joos et al. 2012; A. Frank et al. 2014; J. Bally 2016). This feedback significantly influences both the structure of molecular clouds and the overall efficiency of star formation.

Several theoretical models have been proposed to explain the launching of protostellar outflows, including the X-wind model (F. Shu et al. 1994) and the mag-

netic tower model (D. Lynden-Bell 1996). Among these, the magnetocentrifugal disk wind model has emerged as the leading paradigm (R. D. Blandford & D. G. Payne 1982; R. E. Pudritz & C. A. Norman 1983). In this model, open magnetic field lines thread the surface layers of a Keplerian accretion disk, allowing gas to be centrifugally accelerated outward, forming a characteristic bipolar outflow composed of a fast, collimated jet and a slower, wide-angle wind. This mechanism has been extensively investigated through sophisticated magnetohydrodynamic (MHD) simulations incorporating diverse physical effects and environmental conditions (e.g., R. Ouyed et al. 2003; O. Gressel et al. 2015; G. Mattia & C. Fendt 2020; A. L. Rosen 2022).

A growing body of observational evidence, particularly from high-resolution facilities such as ALMA, supports this model in low- and intermediate-mass protostars. Observations reveal outflows with rotating molecular gas and conical wind morphologies, consistent with predictions from MHD disk wind theory (e.g., R. Launhardt et al. 2009; P. Bjerkeli et al. 2016; A. de Valon et al. 2022; R. Launhardt et al. 2023). These findings suggest that magnetocentrifugal launching may be a universal mechanism operating across a broad range of stellar masses.

Despite these advances, the formation of high-mass stars remains less well understood due to the scarcity of nearby examples, their rapid evolution, and strong radiative feedback. Nevertheless, observations show that massive protostars also launch powerful, collimated outflows resembling scaled-up versions of their low-mass counterparts (e.g., D. S. Shepherd & E. Churchwell 1996; H. Beuther et al. 2004; R. Fedriani et al. 2019; Y. Zhang et al. 2019a; Y. Cheng et al. 2025). Among the various theoretical models for massive star formation, i.e., core accretion, competitive accretion, and stellar collisions, the Turbulent Core Accretion (TCA) model (C. F. McKee & J. C. Tan 2002, 2003; Y. Zhang & J. C. Tan 2011; Y. Zhang et al. 2013, 2014; Y. Zhang & J. C. Tan 2018) offers a physically motivated extension of low-mass star formation theory, wherein massive, turbulent, magnetized, gravitationally bound cores collapse to form massive stars via disk-mediated accretion (see J. C. Tan et al. 2014, for a review).

To explore the impact and appearance of protostellar outflows in this model, a series of 3D MHD simulations were carried out by J. E. Staff et al. (2019, 2023) (hereafter Papers I and II). These simulations follow the collapse of a $60 M_{\odot}$ core embedded in a 1 g cm^{-2} clump, tracking the time evolution of the disk-outflow system as the protostar grows from ~ 1 to $\sim 24 M_{\odot}$. The simulations capture both the structural and kinematic

evolution of the magnetocentrifugal disk wind and its interaction with the infalling envelope, offering a rich, physically consistent dataset for comparison with observations.

To bridge theory and observation, Paper III in this series (D. Xu et al. 2024) conducted radiative transfer post-processing of the simulations to produce synthetic CO line emission data, including position-position-velocity (PPV) cubes and spectra. These were further processed with CASA to simulate realistic ALMA observations. The resulting synthetic spectra were shown to closely reproduce the features of real ALMA-observed protostellar outflows. By comparing synthetic and observed spectra, Paper III derived best-fit protostellar masses and inclination angles for several real systems. However, the approach was based solely on 1D spectral profiles, without incorporating the rich morphological information present in 2D integrated intensity maps of the red- and blue-shifted outflow lobes. This limitation motivates the development of more comprehensive methods that can simultaneously interpret both the spectral and spatial dimensions of the data.

Recent progress in deep learning has provided powerful new tools for inferring the intrinsic physical properties of astrophysical systems from observational data. Convolutional Neural Networks (CNNs) have been successfully applied in various astronomical contexts, particularly for identifying complex spatial structures. For example, the Convolutional Approach to Structure Identification (CASI), which is based on CNNs, has demonstrated the ability to detect stellar feedback features such as winds and outflows, and to estimate their associated mass, energy, and momentum from observations (D. Xu et al. 2020a,b). Similarly, CNNs have been used to predict the orientation of magnetic fields by analyzing gas morphology (D. Xu et al. 2023a). In addition to CNNs, other machine learning frameworks such as Denoising Diffusion Probabilistic Models (DDPMs) have also shown strong potential for recovering physical quantities from observational data that are noisy or incomplete. These models have been applied to infer a range of important parameters, including volume density (D. Xu et al. 2023c), the strength of the interstellar radiation field (D. Xu et al. 2023b), and magnetic field strength (D. Xu et al. 2025), often with higher accuracy than traditional inversion techniques.

Despite the success of CNNs, their reliance on local kernels can limit their ability to capture long-range spatial dependencies in large-scale structures. This has motivated the adoption of Vision Transformers (ViTs) (A. Dosovitskiy et al. 2020), which utilize self-attention to prioritize global geometric context.

The AstroLinformer framework recently demonstrated that transformer-augmented models outperform standard convolutional methods at recovering physical parameters from degraded images, maintaining high robustness despite significant noise and resolution loss (V. Vasudev et al. 2025).

Furthermore, as these models move toward deployment on real observational surveys, the need for rigorous Uncertainty Quantification (UQ) has become paramount to ensure scientific reliability. Modern frameworks increasingly aim to distinguish between inherent data noise (aleatoric) and model-driven uncertainty (epistemic) (A. Kendall & Y. Gal 2017). Probabilistic frameworks like PNet and mixture density networks are increasingly used to provide calibrated error estimates and probability density functions for astronomical parameters (R. Sun et al. 2023; J. Expósito-Márquez et al. 2023). These approaches allow researchers to navigate physical degeneracies and identify when predictions are poorly constrained by the available data.

Building on these advancements, we introduce a multi-modal deep learning framework designed to infer the physical properties of protostellar outflows from observational data. This approach leverages both spatial and spectral information, enabling the model to jointly capture the morphological and kinematic signatures of outflows. The framework is trained on synthetic observations generated from MHD simulations of massive star formation, which offer physically consistent datasets with known ground-truth parameters. By learning the mapping between observational features and intrinsic properties, the model provides a robust and scalable alternative to traditional fitting techniques.

As Paper V in this series, following Paper IV’s computation of radio emission from shock-ionized structures in the outflows (E. C. Gardiner et al. 2024), this work advances automated, data-driven analysis of protostellar outflows. The paper is organized as follows: §2 details the simulation setup, synthetic data generation, and the multi-modal machine learning architecture; §3 presents the results, evaluates model performance, and provides interpretable analysis of feature contributions; §4 applies the framework to real ALMA observations; and §5 summarizes the key findings and outlines directions for future work.

2. DATA AND METHOD

2.1. Magnetohydrodynamics Simulations

We utilize the 3D ideal MHD simulations from J. E. Staff et al. (2023), which model a disk wind outflow from a massive protostar. These simulations follow the Tur-

bulent Core Accretion (TCA) model (C. F. McKee & J. C. Tan 2003), with boundary conditions of the simulations tracking the self-consistent evolution of a protostar growing from $1 M_{\odot}$ to over $24 M_{\odot}$ within an initial $60 M_{\odot}$ core embedded in a clump with $\Sigma_{\text{cl}} = 1 \text{ g cm}^{-2}$ (Y. Zhang et al. 2014). The original simulation domain covers a single hemisphere of the outflow, extending from an injection surface 100 au above the disk to a distance of 26,500 au. For the analysis in this work, we mirror the simulation domain across the disk mid-plane ($x_1 = 0$) to construct a complete, bipolar outflow. A comprehensive description of the MHD simulation setup, code, and parameters can be found in J. E. Staff et al. (2023). In this study, we adopt the same simulation snapshots as those used by D. Xu et al. (2024), corresponding to protostellar masses of 2, 4, 8, 12, 16, 20, and $24 M_{\odot}$.

2.2. Synthetic Observations

We use the publicly available radiative transfer code RADMC-3D (C. P. Dullemond et al. 2012) to generate synthetic ^{12}CO (2-1) spectra under non-LTE conditions. Level populations are computed based on local density and temperature, assuming that gas and dust temperatures are coupled. This assumption is valid for the dense regions ($n_{\text{H}} \gtrsim 10^5 \text{ cm}^{-3}$) that dominate our simulation domain, and dust temperatures are calculated as described in D. Xu et al. (2024). We also conduct radiative transfer from 20 different viewing angles, where the inclination angles are sampled by uniformly spacing the cosine of inclination angles between 0.025 and 0.975, ensuring even coverage over the spherical coordinate system.

To simulate ALMA observations, we post-process the synthetic line data using CASA/`simalma`, adopting the same C36-3 array configuration and 210-second integration time as used in the real observations discussed in §4. To diversify the training set, we include synthetic sources at distances of 500 pc, 1 kpc, and 2 kpc, using 2 kpc as the fiducial setup. While one real observed source lies at 8.4 kpc (see §4), the model’s input images and spectra are normalized, making the training process largely insensitive to distance, as also supported by D. Xu et al. (2024). Figure 1 presents examples of synthetic outflows generated for various protostellar masses and inclination angles. Additional collections of synthetic outflow images are available in D. Xu et al. (2024).

The input to the machine learning model includes a three-channel image: blue-shifted and red-shifted ^{12}CO (2-1) integrated intensities, along with the total integrated intensity, each normalized between 0 and 1. The corresponding spectrum is clipped at $\pm 50 \text{ km/s}$ and sim-

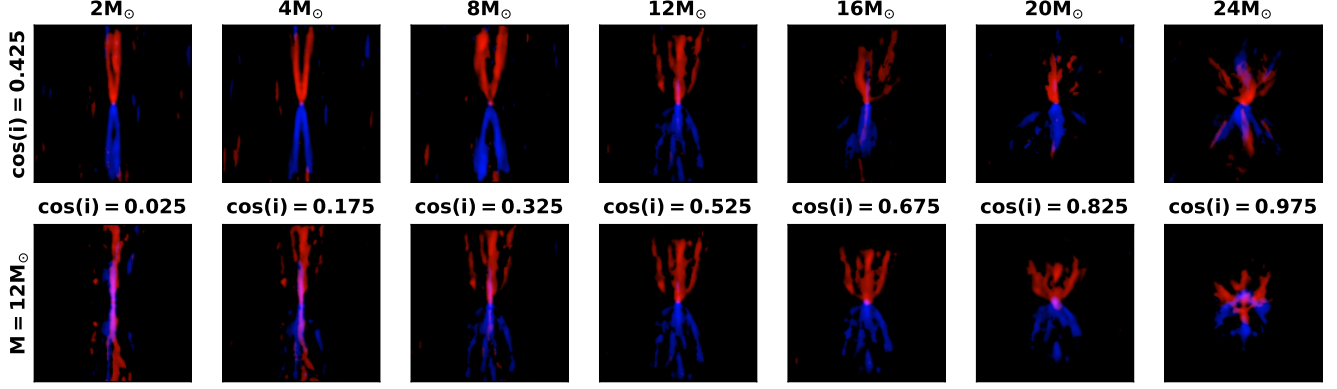


Figure 1. Examples of synthetic outflows with different protostellar masses and inclination angles. Blue represents the blue-shifted outflow lobes ($-50 < v_{blue} < -3 \text{ km s}^{-1}$), while red represents the red-shifted lobes ($3 < v_{red} < 50 \text{ km s}^{-1}$).

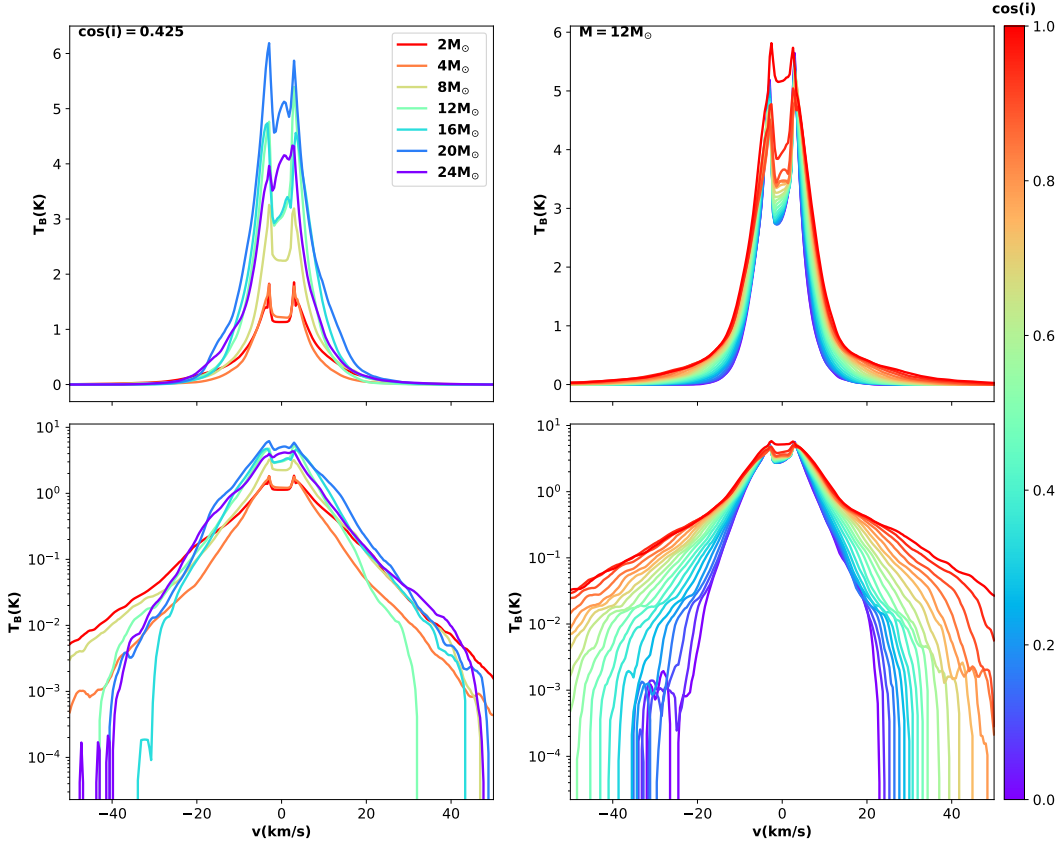


Figure 2. Examples of synthetic outflow spectra for different protostellar masses and inclination angles. The upper panels show the spectra in linear scale, while the lower panels display them in logarithmic scale.

ilarly normalized. To augment the dataset, we implement several strategies in the data loader: randomly shifting the outflow center in the image, swapping the blue- and red-shifted lobes in velocity, rotating the outflow by random position angles, adding Gaussian noise to the image, and injecting pattern noise from other outflows to mimic complex structures. The added pattern noise is at least a factor of three weaker than the main

signal. In addition, we introduce random spectral shifts of $\pm 5 \text{ km/s}$ to simulate velocity-centering uncertainties commonly encountered in real observations.

2.3. Multi-Modal Machine Learning Framework

We present a novel multi-modal machine learning framework that jointly processes spatial and spectral data to infer the physical properties of protostellar out-

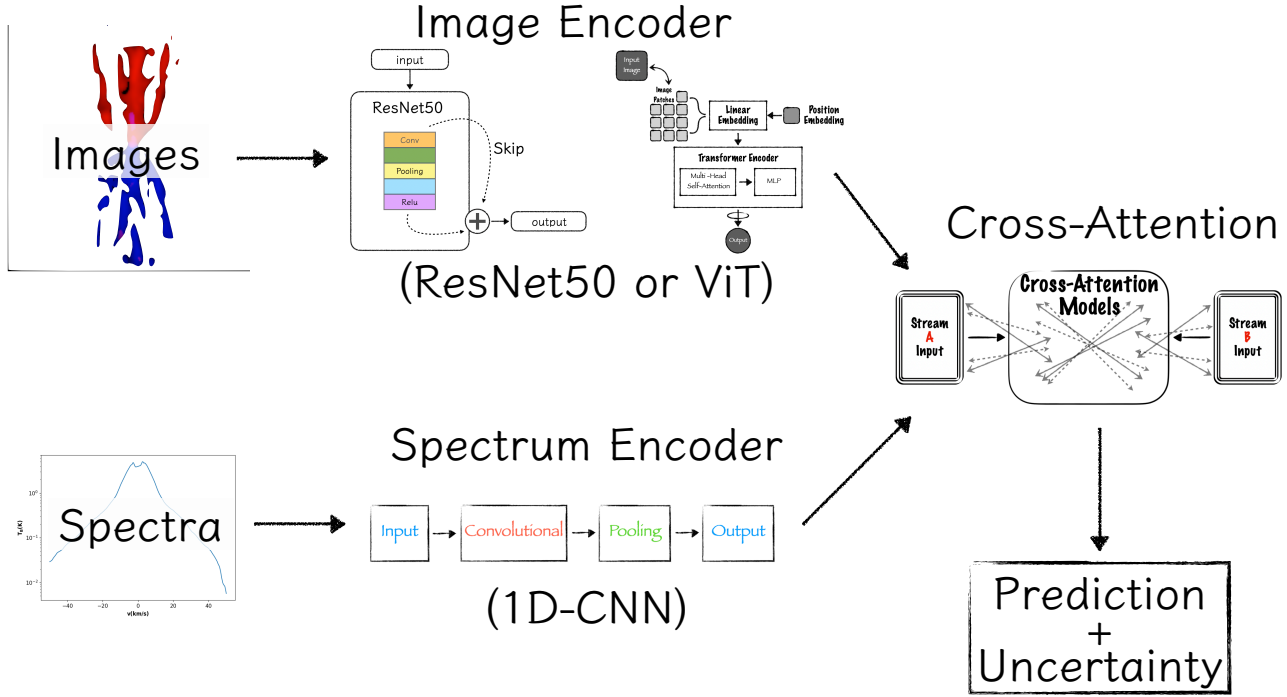


Figure 3. Illustration of the multi-modal machine learning architecture. Image and spectrum encoders extract spatial and spectral features, which are fused via a cross-attention module to produce parameter predictions with associated uncertainties.

flows. The framework consists of two main components: an image encoder and a spectrum encoder. For the image encoder, we adopt widely used pretrained architectures, including ResNet50 (K. He et al. 2016) and ViT_L16 (A. Dosovitskiy et al. 2020), which are effective at extracting high-level spatial features from images. To enable a fair comparison across architectures, we also include ResNet152 and ViT_B_16, which have comparable numbers of parameters. In all cases, we use the feature representations extracted prior to the final classification layer, thereby preserving the embedded information from the input images. The spectrum encoder is designed from scratch using a 1D CNN to learn feature representations of the spectral profile, providing complementary kinematic information. To integrate these two modalities, we employ a cross-attention mechanism that fuses spatial and spectral features. The combined representation is then passed to a multi-layer perceptron (MLP), which performs the final prediction. To move beyond point estimates and quantify predictive confidence, we adopt a probabilistic regression approach. Instead of predicting a single output value, the model learns the parameters of a Gaussian probability distribution: the mean (μ) and variance (σ^2). This enables the model to capture aleatoric uncertainty, the uncertainty intrinsic to the data. For example, noisy spectra or ambiguous image features naturally lead to

higher predicted uncertainty (larger σ). Since the variance must always be positive, the network predicts the log-variance $s = \ln(\sigma^2)$ instead of σ^2 directly. This improves numerical stability and ensures valid outputs. The model is trained by minimizing the Gaussian Negative Log-Likelihood (NLL) of the true value y given the predicted mean μ and log-variance s . After dropping constants, the loss function for a single prediction is:

$$\mathcal{L}(y, \mu, s) = \frac{1}{2} ((y - \mu)^2 e^{-s} + s). \quad (1)$$

This formulation encourages accurate predictions (through the $(y - \mu)^2$ term), while allowing the model to adjust its predicted variance for inputs with higher inherent uncertainty. The final model thus outputs both predictions and a principled measure of confidence. An overview of the architecture is shown in Figure 3. To further enhance robustness to real-world data imperfections, we introduce a random masking strategy in the spectrum encoder. During training, random segments of the input spectrum are set to zero, mimicking missing or corrupted spectral channels that often arise in observations.

The model is trained to predict three key physical properties for each input sample: protostellar mass, inclination angle, and position angle. The mass ranges from 2 to $24 M_{\odot}$, the inclination angle from 0° to 90° ,

and the position angle from -90° to $+90^\circ$. All outputs are normalized to improve training stability. To handle the circular nature of the position angle, we represent it as a two-component vector using sine and cosine values. This avoids discontinuities near $\pm 90^\circ$, which can confuse standard regression.

We follow a progressive fine-tuning approach during training. In the first stage, we freeze the image encoder and train only the spectrum encoder, cross-attention module, and MLP using a relatively high learning rate. After the validation loss fails to improve for 10 consecutive epochs, we unfreeze the last layer of the image encoder and continue training with a lower learning rate. In the final stage, we unfreeze all model parameters and reduce the learning rate further. Training continues until the validation error stops decreasing for another 10 epochs. We save the model with the best validation performance as our fiducial model.

Besides the fiducial model training on all the physical parameters, we also conduct test model training which only includes certain physical setups. In particular, in these test models we exclude all samples with a protostellar mass of $12 M_\odot$, and also exclude all samples with five specific inclination angles (with cosine values 0.125, 0.325, 0.525, 0.725 and 0.925), which means the training data does not cover any of these parameters, reducing the total training sample by 35%. This test model aims to show the how the model performs with limited dataset and, especially, the ability to predict properties of unseen data.

3. RESULTS

3.1. Assessing Model Performance

We evaluate the performance of the trained multi-modal machine learning models using synthetic test datasets, beginning with an assessment of generalization under limited training coverage. In this setup, we exclude all samples with a protostellar mass of $12 M_\odot$ and five specific inclination angles from the training phase, evaluating the models exclusively on these unseen parameter combinations. Figure 4 illustrates the performance of the ViT_L_16 architecture; for conciseness, the comparative results for all four model architectures are detailed in Figure 13 of Appendix A. A common limitation observed across all models is the discretization of predictions resulting from the sparse sampling of the physical parameter space. Consequently, predictions for the unseen $12 M_\odot$ case tend to cluster around the nearest training grid points (e.g., 8, 16, or $24 M_\odot$). However, the error distributions reveal distinct behaviors between architectures: ViT-based models systematically bias predictions toward $16 M_\odot$, suggesting an ability

to capture the continuous evolutionary progression of outflow morphology. In contrast, ResNet-based models exhibit broader, less structured biases, likely reflecting intrinsic morphological degeneracies exacerbated by beam convolution and noise. Despite these challenges in mass and inclination recovery, the position angle remains a robustly diagnosable parameter, with all four models achieving accurate recovery even for previously unseen outflow configurations.

We next evaluate the fiducial models, which are trained on the full range of protostellar masses and inclination angles using the 1 kpc and 2 kpc datasets. Testing is conducted on the reserved 500 pc dataset, utilizing a fixed set of position angles sampled at 30° intervals to ensure consistent evaluation. Figure 5 summarizes the results for the ViT_L_16 model; for conciseness, comparative results for all four architectures are detailed in Figure 14 of Appendix A. Across the board, all models achieve accurate predictions for mass, inclination, and position angle, characterized by low bias and small uncertainties. Despite significant differences in model complexity—ranging from $\sim 27M$ parameters for ResNet50 to $\sim 307M$ for ViT_L_16—overall performance is broadly comparable, indicating that increasing model size does not yield uniform improvements. As shown in the Appendix, ResNet152 slightly underperforms the smaller ResNet50, suggesting potential overparameterization relative to the training data. In contrast, the ViT-based models prove more robust to scaling, with ViT_L_16 outperforming the ResNet architectures, particularly in protostellar mass prediction.

We then assess model robustness to resolution degradation by testing performance on synthetic data convolved with increasingly large Gaussian kernels. Figure 6 illustrates the performance of ViT_L_16, while comparative results for all four architectures are provided in Figure 15 of Appendix A. Although training augmentations included Gaussian smoothing with σ between 0.75 and 2.0 (for 224×224 inputs), we test well beyond this range. All models experience significant performance degradation when the kernel size exceeds $\sigma \sim 5$, reflecting the inevitable loss of morphological information at extreme smoothing levels. However, ViT_L_16 consistently provides the most stable position angle predictions under heavy blurring. Similarly, ViT_B_16 demonstrates superior generalization compared to ResNet-based models with equivalent parameter counts. These results suggest that transformer-based architectures are particularly well-suited for handling unseen observational conditions and degraded spatial information in protostellar outflow studies.

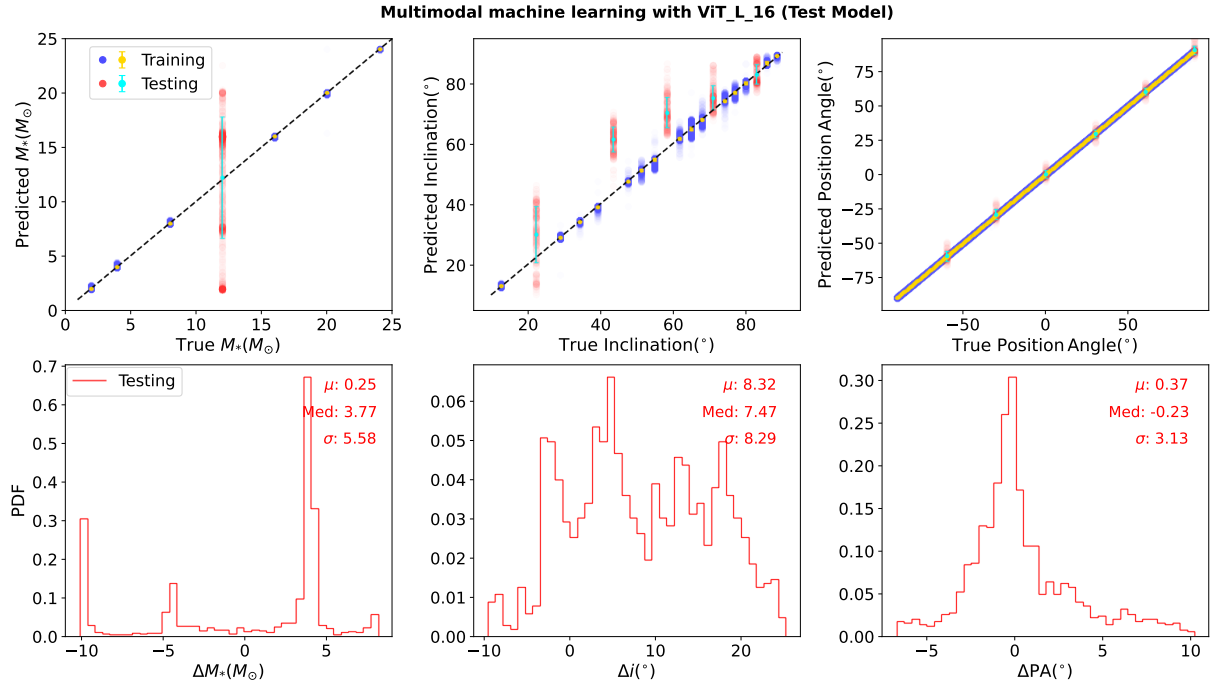


Figure 4. Performance of the ViT_L_16 test model. See Appendix A (Figure 13) for a comparison of other model architectures. This model is trained on a restricted dataset that excludes samples with a protostellar mass of $12 M_\odot$ and five specific inclination angles. Model performance is evaluated on outflows corresponding to the excluded mass and inclination angles. The top row compares the ground-truth values with the model predictions for protostellar mass, inclination angle, and position angle from left to right. The bottom row shows the probability distribution functions (PDFs) of the prediction errors, defined as the difference between the predicted and true values.

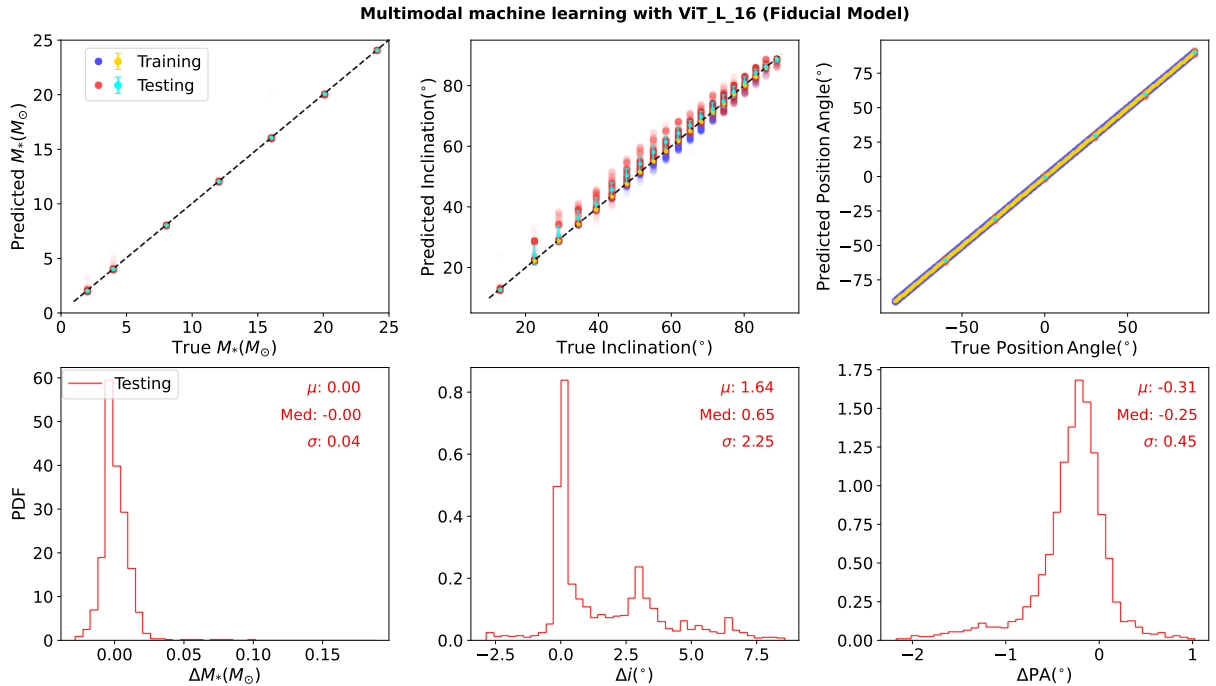


Figure 5. Performance of the ViT_L_16 model, but trained on the full range of protostellar masses and inclination angles.

Finally, we perform a controlled ablation test to isolate the contribution of the spectral modality. As de-

tailed in § 2.3, our training strategy involved randomly

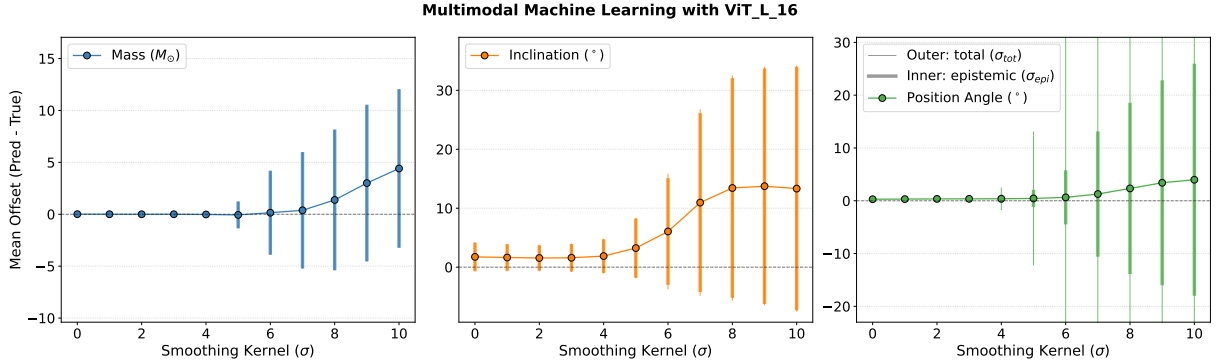


Figure 6. Performance of the ViT_L-16 model on synthetic data convolved with progressively larger Gaussian kernels. From left to right, panels show results for protostellar mass, inclination angle, and position angle, including predicted means, total uncertainties, and epistemic (model) uncertainties. The total uncertainty is computed as the quadrature sum of epistemic and aleatoric (data) uncertainties.

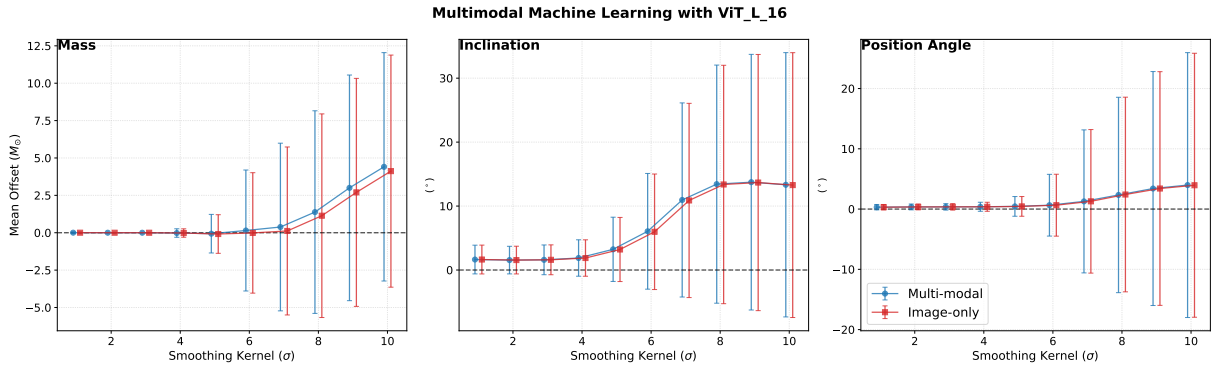


Figure 7. Comparison of the ViT_L-16 model performance for two input configurations: multi-modal (images + spectra) and image-only, evaluated on synthetic data with progressively increased Gaussian smoothing.

masking spectral segments, explicitly encouraging the network to prioritize spatial features. To evaluate this at inference, we disable the spectral branch entirely (setting inputs to zero) and compare performance against the standard multi-modal baseline. Figure 7 illustrates the results for ViT_L-16, while comparative plots for all four architectures are provided in Figure 16 of Appendix A. The results reveal architecture-dependent sensitivities. For ResNet-based models, including spectra improves inclination angle predictions but slightly degrades mass estimates, leaving position angles largely unaffected. Conversely, ViT_B-16 sees a modest improvement in mass prediction from spectral data with minimal impact on other parameters. Interestingly, for ViT_L-16, the inclusion of spectra results in a slight performance dip for both mass and inclination. This suggests that for this larger backbone, spectral features may introduce mild confusion under the current training setup, or potentially reflects test-set variance; regardless, position angle recovery remains robust across all configurations, confirming it is driven almost exclusively by spatial morphology. Overall, under moderate

blurring conditions ($\sigma \lesssim 4$), model performance remains virtually unchanged whether spectral data is included or not. This behavior is consistent with our training strategy and corroborates the Integrated Gradients analysis in §3.2, confirming that spatial features are the dominant drivers of the predictions.

3.2. Interpretable Analysis of Physical Feature Contributions in the Multi-Modal Network

To interpret the decision-making process of our multi-modal neural network and to quantify how specific spatial and spectral features contribute to both the predicted outflow properties (the mean, μ) and their associated uncertainties (the variance, σ^2), we employ three complementary interpretability techniques: Smooth Grad-CAM++, Integrated Gradients (IG), and Occlusion Sensitivity Analysis. Together, these methods provide insight into model behavior at different levels, from coarse localization of salient regions to fine-grained attribution and direct causal testing through perturbation.

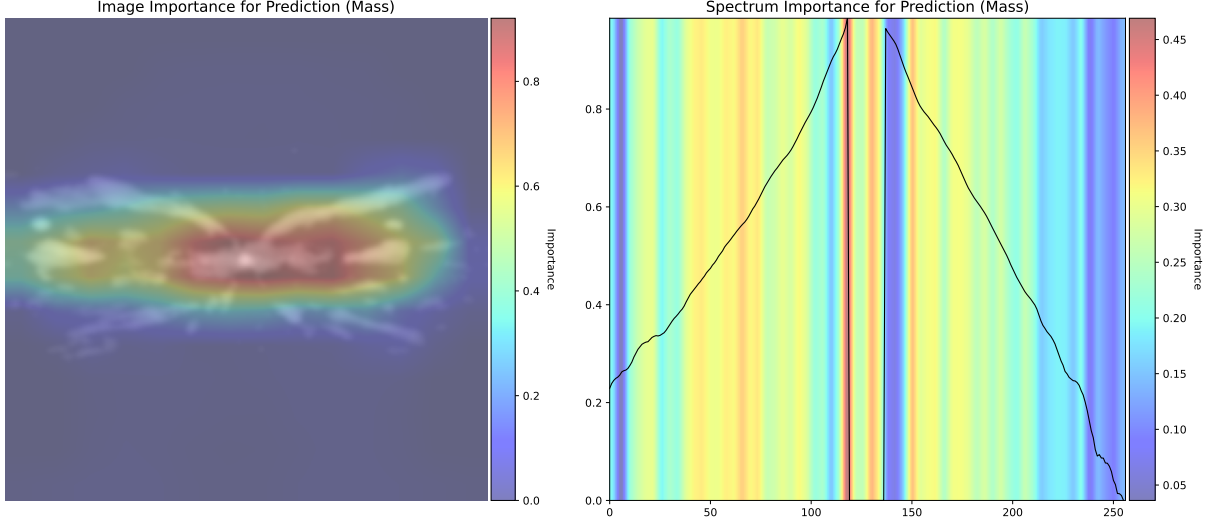


Figure 8. Grad-CAM++ visualizations for outflow mass prediction using the ViT_L-16 model. The background shows the corresponding test outflow input, image (left) and spectrum (right). The overlaid heatmaps indicate regions that contribute most strongly to the inferred quantities.

3.2.1. Smooth Grad-CAM++ Visualization

We first apply Smooth Grad-CAM++, an enhanced gradient-based localization method, to visualize which regions of the input images and spectra most strongly influence the model’s predictions. Compared to standard Grad-CAM, the Grad-CAM++ formulation incorporates pixel-wise weighting of higher-order gradients, allowing it to better capture multiple active regions and complex spatial structures that are particularly relevant for extended objects such as protostellar outflows. To further reduce stochastic noise inherent in single-pass gradient maps, we adopt a SmoothGrad-style approach by averaging Grad-CAM++ maps over multiple noisy realizations of the input ($N = 10$), with gradients explicitly enabled for our regression targets.

The resulting heatmaps highlight physically meaningful structures, including central outflow regions, cavity walls, and terminal lobes—that drive the model’s inference. Figure 8 displays representative Grad-CAM++ visualizations for outflow mass prediction using the ViT_L-16 model. A comprehensive comparison, including uncertainty maps and corresponding results for ResNet50, is available in Figure 17 of Appendix B.

We find that both architectures primarily attend to the central outflow and cavity regions when predicting mass, consistent with the expectation that mass is encoded in the overall spatial extent and intensity distribution of the flow. However, distinct attention strategies emerge for position angle prediction (specifically the cosine term), as detailed in Appendix B (Figure 18). While the ResNet50 model focuses sharply on the edges and distal regions of the outflow cavities, ViT_L-16 as-

signs importance to a broader spatial context, including the void regions surrounding the outflow. This behavior is physically intuitive, as the outflow axis is defined as much by the geometry of the surrounding low-emission regions as by the emitting material itself.

In principle, spectral information should contribute minimally to position angle estimation, since the spectral line shape varies primarily with protostellar mass and inclination angle, while remaining invariant under rotation in the plane of the sky. However, this separation is not always clearly reflected in the Grad-CAM++ visualizations. This limitation arises from several factors. First, Grad-CAM++ operates on intermediate feature maps rather than directly on input pixels, which can obscure modality-specific contributions after multi-modal fusion. Second, the use of higher-order gradients makes the method sensitive to indirect correlations learned during training, even when those correlations are weak or non-causal. Finally, because the model jointly predicts both μ and σ , gradient signals may reflect uncertainty estimation pathways rather than direct physical dependence. These effects motivate the use of a more quantitative attribution method, which we explore next using Integrated Gradients.

3.2.2. Integrated Gradients with Mean Baseline

To obtain pixel-level and channel-level attribution with stronger theoretical guarantees, we apply Integrated Gradients (IG). This method assigns an importance score to each input feature by integrating the gradients of the output along a straight-line path from a baseline input to the actual input. Unlike gradient-only methods, IG satisfies the completeness axiom, ensuring

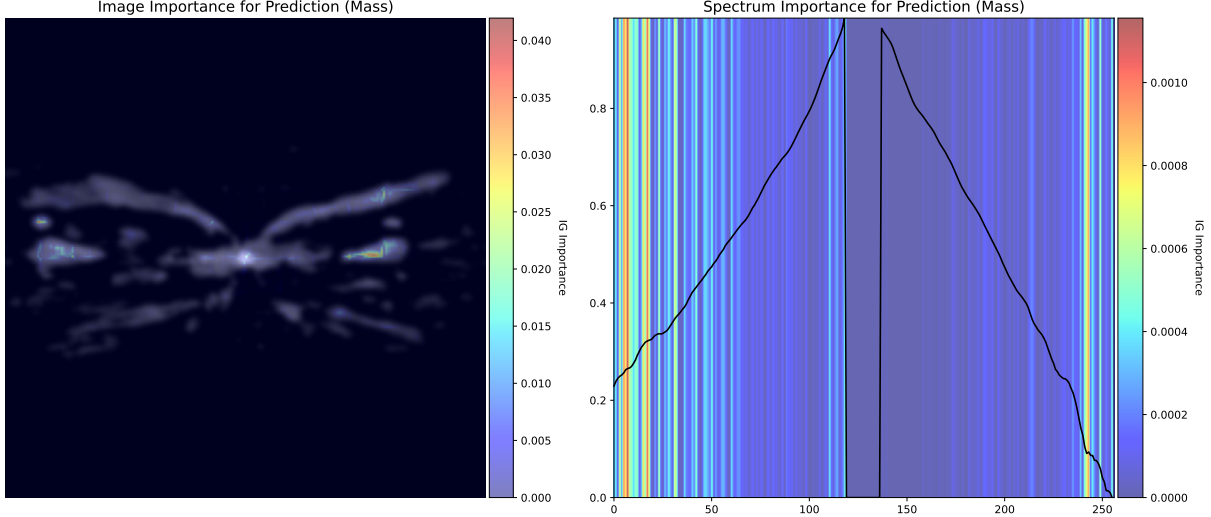


Figure 9. Same as Figure 8, but showing Integrated Gradients maps for the prediction of outflow mass using the ViT_L_16 model.

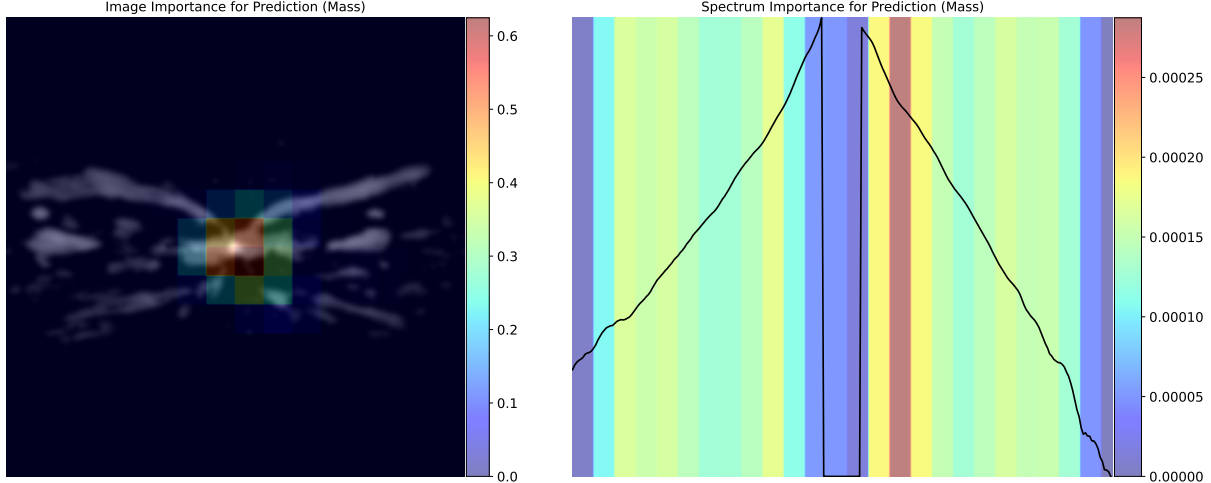


Figure 10. Same as Figure 8, but showing Occlusion Sensitivity Analysis results for outflow mass prediction using the ViT_L_16 model.

that the sum of all attributions equals the difference between the model output and its baseline prediction.

We adopt the mean image and mean spectrum of the training dataset as the baseline, rather than a zero-valued input. This choice defines a physically meaningful reference state corresponding to an average protostellar environment, allowing attributions to be interpreted as deviations from typical conditions rather than from an artificial null input. By integrating gradients over 30-50 interpolation steps, we obtain stable and high-resolution importance maps for both spatial and spectral inputs.

Figure 9 displays representative Integrated Gradients maps for mass prediction using the ViT_L_16 model. For a complete comparison, including ResNet50 results,

position angle predictions, and associated uncertainty maps, refer to Figures 19 and 20 in Appendix B. The analysis confirms that for both architectures, the dominant contributions stem from central outflow regions and cavity edges. While consistent with the Grad-CAM++ results, IG offers clearer modality separation, revealing that attributions associated with spectral input are systematically weaker than those derived from the images. This contrast is most pronounced in position angle predictions, where the spectral contribution is minimal, and nearly negligible for ViT_L_16. This behavior aligns with physical expectations, confirming that the model correctly isolates spatial morphology as the primary driver for inferring orientation on the plane of the sky.

Table 1. Integrated Gradients (IG) Importance Scores by Modality and Architecture

Model	Modality	Mass		Inclination		PA (cos)		PA (sin)	
		Mean	Uncert.	Mean	Uncert.	Mean	Uncert.	Mean	Uncert.
ResNet50									
Image		0.0466	0.3176	0.0494	0.2245	0.0455	0.1861	0.0520	0.5744
Spectrum		0.0024	0.1229	0.0092	0.0712	0.0018	0.0546	0.0027	0.2187
ViT_L_16									
Image		0.1057	9.0×10^{-6}	0.0612	1.4397	0.0805	2.3669	0.0792	2.0430
Spectrum		0.0011	1.0×10^{-6}	0.0016	0.4006	0.0001	0.1886	0.0001	0.2701

NOTE—Importance scores represent the Average L_2 Norm of the Integrated Gradients. The “Uncert.” columns refer to the importance attributed to the model’s predicted $\ln(\sigma^2)$ for each physical parameter.

To assess modality importance statistically, we compute the average IG attribution across the full test set of 6,720 samples for each predicted quantity. Table 1 summarizes the relative contributions of image and spectral inputs for the ResNet50 and ViT_L_16 models. In all cases, spatial information dominates the prediction of physical properties. The spectrum plays a secondary but non-negligible role in predicting protostellar mass and inclination angle, particularly for ViT_L_16, while its contribution to position angle prediction remains minimal for both architectures.

When examining uncertainty predictions, images again dominate the IG attributions. However, in some cases, the spectral input shows increased importance for the uncertainty associated with position angle predictions. This behavior likely reflects the structure of the probabilistic loss function, in which uncertainty estimation is coupled to residual errors in the mean prediction. When spatial cues for position angle are strong, the model may rely on subtle spectral variations to modulate its confidence, even if those variations are not directly informative for the angle itself. In addition, uncertainty pathways in the network can amplify weak correlations that are otherwise suppressed in mean predictions, leading to higher apparent spectral importance in σ than in μ .

3.2.3. Occlusion Sensitivity Analysis

Finally, we perform Occlusion Sensitivity Analysis to test the causal relevance of the features identified by gradient-based methods. In this approach, we systematically mask localized patches of the input image and segments of the spectrum using the dataset mean, and measure the resulting changes in both the predicted mean and uncertainty. Unlike attribution methods, occlusion

directly probes how the removal of information affects model outputs.

Figure 10 presents representative occlusion sensitivity results for mass prediction using the ViT_L_16 model. For a comprehensive comparison, including results for position angle and uncertainty estimates across both ResNet50 and ViT_L_16 architectures, refer to Figures 21 and 22 in Appendix B. The analysis reveals that both architectures exhibit strong sensitivity to the masking of central outflow regions, cavity edges, and terminal lobes, confirming the causal importance of these structures for accurate inference. In contrast, occluding spectral segments produces comparatively minor changes in the model output, providing further independent support for the conclusions drawn from the Integrated Gradients analysis.

The strong agreement across Smooth Grad-CAM++, Integrated Gradients, and Occlusion Sensitivity Analysis provides robust evidence that the model’s predictions are grounded in physically interpretable features of protostellar outflows. Together, these results demonstrate that the multi-modal framework not only achieves high predictive accuracy but also learns representations that are consistent with established physical intuition about outflow morphology and kinematics.

4. APPLICATION TO REAL ALMA-OBSERVED PROTOSTELLAR OUTFLOWS AND UNCERTAINTY ASSESSMENT

In this section, we apply our trained multi-modal machine learning models to real ALMA observations of protostellar outflows in order to assess model robustness and physical plausibility beyond the synthetic domain. We analyze ^{12}CO (2-1) emission from three massive protostellar objects: G35.200.74N (hereafter G35.20;

Á. Sánchez-Monge et al. 2013; Y. Zhang et al. 2022), G45.47+0.05 (hereafter G45.47; Y. Zhang et al. 2019b), and G339.881.26 (hereafter G339.88; Y. Zhang et al. 2019a). Their distances are 2.2 kpc, 8.4 kpc, and 2.1 kpc, respectively.

The ^{12}CO (2-1) data were obtained with ALMA in the C36-3 configuration in 2016 (project ID: 2015.1.01454.S), with baselines ranging from 15 m to 463 m and an on-source integration time of 3.5 minutes per target. The synthesized beams have major axes of 0.87'', 0.90'', and 0.93'', and minor axes of 0.83'', 0.84'', and 0.74'' for G35.20, G45.47, and G339.88, respectively. Data calibration and imaging were performed in CASA. After standard pipeline calibration, self-calibration using the continuum was applied to the CO line data, and imaging was carried out with the tclean task using Briggs weighting with robust = 0.5. We refer readers to the original publications for full observational details.

4.1. Rotation-Based Evaluation and Uncertainty Decomposition

To test model robustness and quantify predictive uncertainty on real observations, we exploit rotational augmentation at inference time. For each source, we rotate the outflow image by steps of 3° , producing 120 rotated versions that are independently passed through the trained models. This strategy enables us to separate two distinct uncertainty components:

1. Aleatoric uncertainty, obtained directly from the model output through the predicted $\ln(\sigma^2)$, reflects irreducible noise inherent to the data, such as finite angular resolution, instrumental noise, projection effects, and confusion from overlapping structures along the line of sight.
2. Epistemic uncertainty, estimated from the dispersion of predicted means across rotations, captures model sensitivity to input orientation and thus reflects limitations in model generalization and feature robustness.

Ideally, physical quantities such as mass and inclination should be invariant under image rotation. Therefore, any systematic variation in predictions across rotations indicates residual orientation sensitivity in the learned representations.

Several factors can contribute to rotation-dependent prediction variability, even for a well-trained model. First, pixel interpolation during rotation introduces small but non-negligible changes in local textures and sharp edges, which can affect feature extraction. Second, standard convolution kernels and patch embeddings are not intrinsically rotation-invariant, meaning

that rotated structures activate different filters or attention patterns. Third, aliasing of fine-scale ISM substructure can create artificial high-frequency features after rotation, which the network may interpret as physical morphology.

For each of the N rotated inputs, the model predicts a mean μ_i and variance σ_i^2 . We compute the final prediction and uncertainty as:

$$\mu_{\text{final}} = \frac{1}{N} \sum_{i=1}^N \mu_i, \quad (2)$$

$$\sigma_{\text{total}}^2 = \underbrace{\frac{1}{N} \sum_{i=1}^N \sigma_i^2}_{\text{mean aleatoric}} + \underbrace{\frac{1}{N} \sum_{i=1}^N (\mu_i - \mu_{\text{final}})^2}_{\text{epistemic (rotational dispersion)}}. \quad (3)$$

This formulation ensures that the total uncertainty remains large if the model is internally confident but inconsistent under rotation, providing a more realistic assessment than a single forward pass.

4.2. Comparison with Previous Estimates

Figure 11 presents the rotation-averaged predictions and uncertainty decomposition for all three sources. The predicted masses for the three outflows cluster around $\sim 12\text{-}15 M_\odot$ with relatively small total uncertainties.

For comparison, R. Fedriani et al. (2023) estimated protostellar masses of $13\text{-}28 M_\odot$ for G35.20, $23\text{-}53 M_\odot$ for G45.47, and $11\text{-}42 M_\odot$ for G339.88 based on SED fitting, with inclination angles of approximately 60° for all three sources. Their inferred initial core masses are significantly higher, ranging from ~ 80 to over $400 M_\odot$.

The primary source of discrepancy is that our training simulations assume a fixed initial core mass of $60 M_\odot$. As a result, the predicted “protostellar mass” from our models should not be interpreted as an absolute physical mass for real systems, but rather as a proxy for evolutionary stage within the restricted simulation parameter space. Under this interpretation, the ML-inferred masses for G35.20 and G339.88 are broadly consistent with the evolutionary stages inferred from SED modeling. In contrast, G45.47 appears more evolved than suggested by SED fitting when assessed by the stellar-toinitial-core mass ratio, but less evolved in terms of absolute stellar mass, because its initial core mass inferred from SED modeling ($228\text{-}444 M_\odot$; R. Fedriani et al. 2023) is substantially larger than the fixed initial core mass adopted in our simulations.

The inclination predictions show more pronounced discrepancies. The models infer G35.20 and G45.47 to be relatively pole-on (inclinations $\sim 10\text{-}20^\circ$), whereas G339.88 is predicted to be close to edge-on (inclinations $\sim 70\text{-}80^\circ$). Morphologically, G339.88 indeed exhibits

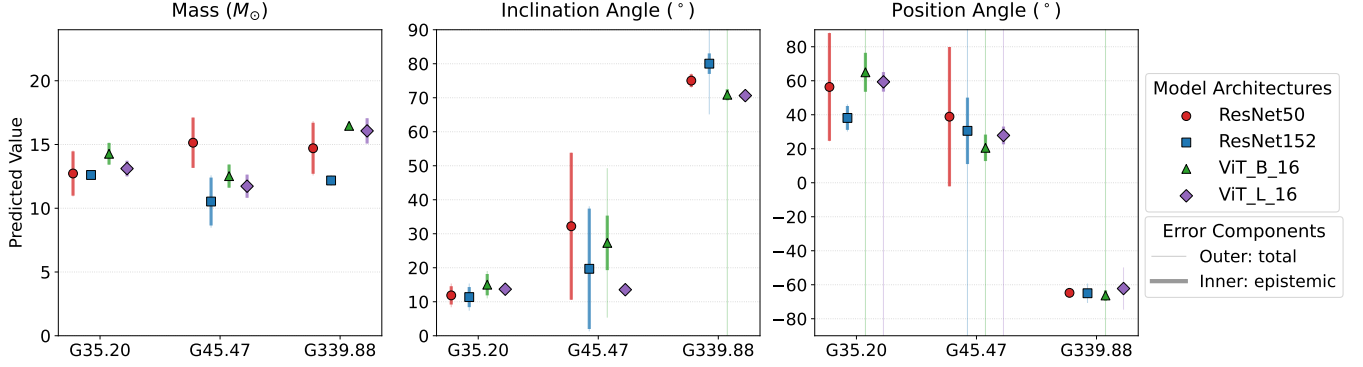


Figure 11. Rotation-averaged predictions for the three ALMA-observed outflows from the four machine learning models, including the predicted means, total uncertainties, and the epistemic component arising from rotational dispersion.

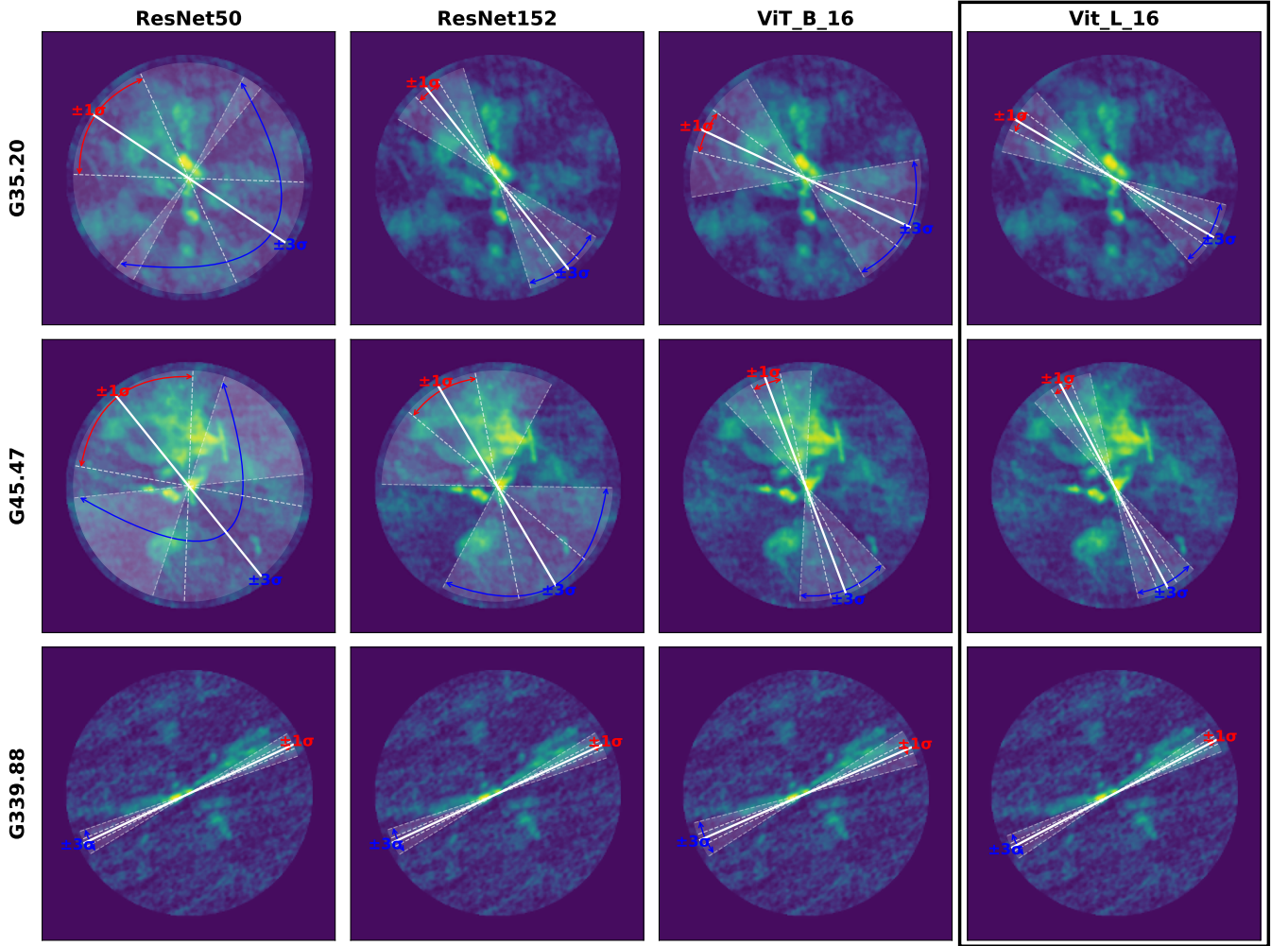


Figure 12. Predicted outflow position angles for the three sources from all four machine learning models, with associated epistemic uncertainties. The background image displays the total ^{12}CO (21) integrated intensity, the solid white line denotes the mean predicted position angle, and the semi-transparent white wedges represent the 1σ and 3σ epistemic uncertainty ranges. The black box highlights the performance of the fiducial ViT model on the three sources.

narrow, well-separated bipolar lobes, consistent with an edge-on configuration, whereas G35.20 and G45.47 dis-

play broader cavities and more complex structures in

the training simulations associated with low-inclination outflows.

In contrast, SED-based studies tend to infer more edge-on viewing angles for G35.20 and G45.47. However, SED fitting is known to suffer from degeneracies between inclination, envelope geometry, and cavity opening angle, and may not uniquely constrain outflow orientation. Indeed, discrepancies between SED modeling and CO spectral profile fitting have also been reported, particularly for G45.47 (D. Xu et al. 2024). This highlights that neither approach should be regarded as definitive in isolation. Furthermore, in the case of G35.20, the region is known to contain multiple protostellar outflows (Y. Zhang et al. 2022), which thus impact the results derived when interpreting as a single, dominant source.

4.3. Position Angle as a Robust Validation Metric

A more direct and visually verifiable quantity is the outflow position angle. Figure 12 shows the position angle predictions from all four models for the three sources, along with their epistemic uncertainties. The mean position angles are broadly consistent across models and align well with the apparent outflow orientations in the images, demonstrating that the networks have successfully learned robust morphological cues associated with bipolar geometry.

While some models exhibit large epistemic or aleatoric uncertainties for specific sources, others achieve high precision, indicating that uncertainty is strongly sample-dependent and model-dependent. The overall consistency in position angle predictions, despite domain shift from simulations to real data, provides encouraging evidence that the models capture physically meaningful outflow structures rather than overfitting to synthetic artifacts.

Together, these results suggest that while absolute physical parameters inferred from the current models should be interpreted cautiously due to limitations in the training parameter space, the models nonetheless extract robust geometric information from real observations and provide physically interpretable uncertainty estimates. This supports the feasibility of extending this framework to more realistic simulations with broader initial conditions in future work.

5. CONCLUSIONS

We have developed a multi-modal machine learning framework that jointly exploits spatial and spectral information to infer the physical properties of protostellar outflows. By coupling image and spectrum encoders through a cross-attention fusion mechanism, the

model integrates morphological and kinematic features in a physically motivated manner. The framework was trained and validated on synthetic observations and successfully applied to real ALMA ^{12}CO (2-1) data. Our main findings are summarized as follows:

1. Across all four backbone architectures evaluated (ResNet50, ResNet152, ViT_B_16, and ViT_L_16), the framework accurately recovers protostellar mass, inclination angle, and position angle. When trained on the full parameter space, all models exhibit low systematic bias and well-constrained uncertainties.
2. Model performance degrades gradually as spatial resolution is reduced via Gaussian smoothing. However, Vision Transformer-based models, particularly ViT_L_16, demonstrate superior robustness under strong blurring. This suggests that the self-attention mechanism is more effective than traditional convolutions at preserving global outflow geometry when fine-scale morphological structures are suppressed.
3. Interpretability analyses using Smooth Grad-CAM++, Integrated Gradients, and Occlusion Sensitivity reveal a physically consistent dependency: spatial features dominate the prediction of all parameters, while spectral profiles provide critical secondary constraints for mass and inclination. The minimal contribution of spectra to position angle estimation aligns with physical expectations, confirming that the model has learned meaningful modality-specific physical correlations.
4. When trained on sparse parameter spaces, ViT-based models show a significantly stronger ability to interpolate physical trends compared to ResNet architectures. This suggests that Transformers are better suited for capturing the continuous evolution of outflows rather than merely memorizing discrete sampled values.
5. By employing a rotation-based uncertainty decomposition on ALMA data, we successfully separated aleatoric (data-driven) and epistemic (model-driven) contributions. We find that mass estimates remain relatively stable, whereas inclination and position angle exhibit larger epistemic scatter in complex sources, providing a more rigorous and realistic measure of model confidence than single-pass predictions.
6. For the analyzed ALMA sources, inferred protostellar masses cluster between $12\text{--}15 M_{\odot}$. These

values are lower than traditional SED-based estimates, reflecting the $60 M_{\odot}$ initial core mass constraint of the training set; thus, these results are best interpreted as indicators of the evolutionary stage. While recovered position angles show excellent agreement with visual morphology, inclination angles exhibit larger discrepancies, highlighting the inherent degeneracies between viewing geometry and evolutionary effects.

Overall, this work demonstrates that multi-modal learning provides a physically interpretable and scalable approach for linking observed outflow signatures to underlying protostellar properties. While the current model is bounded by the physical diversity of the training simulations, the framework is modular and can be extended to broader parameter spaces, additional molecular tracers, and more heterogeneous environments. These developments will facilitate the automated, physi-

cally informed analysis of large-scale ALMA surveys and future high-resolution facilities.

ACKNOWLEDGMENTS

This paper is dedicated to Jan E. Staff (29th May 1977 - 16th May 2023). D.X. acknowledges support from the Virginia Initiative on Cosmic Origins (VICO) and the Natural Sciences and Engineering Research Council of Canada (NSERC), [funding reference number 568580]. D.X. also acknowledges support from the Eric and Wendy Schmidt AI in Science Postdoctoral Fellowship Program, a program of Schmidt Sciences. I.A.S. acknowledges support from a Chalmers Astrophysics and Space Sciences Summer (CASSUM) research fellowship. J.C.T. acknowledges support from NSF grant AST-2206450 and ERC Advanced grant 788829 (MSTAR). J.C.T also acknowledges funding from the Virginia Institute for Theoretical Astrophysics (VITA), supported by the College and Graduate School of Arts and Sciences at the University of Virginia.

REFERENCES

Bally, J. 2016, *ARA&A*, 54, 491, doi: [10.1146/annurev-astro-081915-023341](https://doi.org/10.1146/annurev-astro-081915-023341)

Beuther, H., Schilke, P., & Gueth, F. 2004, *ApJ*, 608, 330, doi: [10.1086/386543](https://doi.org/10.1086/386543)

Bjerkeli, P., van der Wiel, M. H. D., Harsono, D., Ramsey, J. P., & Jørgensen, J. K. 2016, *Nature*, 540, 406, doi: [10.1038/nature20600](https://doi.org/10.1038/nature20600)

Blandford, R. D., & Payne, D. G. 1982, *MNRAS*, 199, 883, doi: [10.1093/mnras/199.4.883](https://doi.org/10.1093/mnras/199.4.883)

Cheng, Y., Tan, J. C., Andersen, M., et al. 2025, *ApJ*, 990, 173, doi: [10.3847/1538-4357/addf4b](https://doi.org/10.3847/1538-4357/addf4b)

de Valon, A., Dougados, C., Cabrit, S., et al. 2022, *A&A*, 668, A78, doi: [10.1051/0004-6361/202141316](https://doi.org/10.1051/0004-6361/202141316)

Dosovitskiy, A., Beyer, L., Kolesnikov, A., et al. 2020, arXiv e-prints, arXiv:2010.11929, doi: [10.48550/arXiv.2010.11929](https://doi.org/10.48550/arXiv.2010.11929)

Dullemond, C. P., Juhasz, A., Pohl, A., et al. 2012, RADMC-3D: A multi-purpose radiative transfer tool,, Astrophysics Source Code Library, record ascl:1202.015 <http://ascl.net/1202.015>

Expósito-Márquez, J., Brook, C. B., Huertas-Company, M., et al. 2023, *MNRAS*, 519, 4384, doi: [10.1093/mnras/stac3799](https://doi.org/10.1093/mnras/stac3799)

Fedriani, R., Caratti o Garatti, A., Purser, S. J. D., et al. 2019, *Nature Communications*, 10, 3630, doi: [10.1038/s41467-019-11595-x](https://doi.org/10.1038/s41467-019-11595-x)

Fedriani, R., Tan, J. C., Telkamp, Z., et al. 2023, *ApJ*, 942, 7, doi: [10.3847/1538-4357/aca4cf](https://doi.org/10.3847/1538-4357/aca4cf)

Frank, A., Ray, T. P., Cabrit, S., et al. 2014, in *Protostars and Planets VI*, ed. H. Beuther, R. S. Klessen, C. P. Dullemond, & T. Henning, 451–474, doi: [10.2458/azu_uapress_9780816531240-ch020](https://doi.org/10.2458/azu_uapress_9780816531240-ch020)

Gardiner, E. C., Tan, J. C., Staff, J. E., et al. 2024, *ApJ*, 967, 145, doi: [10.3847/1538-4357/ad39e1](https://doi.org/10.3847/1538-4357/ad39e1)

Gressel, O., Turner, N. J., Nelson, R. P., & McNally, C. P. 2015, *ApJ*, 801, 84, doi: [10.1088/0004-637X/801/2/84](https://doi.org/10.1088/0004-637X/801/2/84)

He, K., Zhang, X., Ren, S., & Sun, J. 2016, in *2016 IEEE Conference on Computer Vision and Pattern Recognition (CVPR)*, 1, doi: [10.1109/CVPR.2016.90](https://doi.org/10.1109/CVPR.2016.90)

Joos, M., Hennebelle, P., & Ciardi, A. 2012, *A&A*, 543, A128, doi: [10.1051/0004-6361/201118730](https://doi.org/10.1051/0004-6361/201118730)

Kendall, A., & Gal, Y. 2017, arXiv e-prints, arXiv:1703.04977, doi: [10.48550/arXiv.1703.04977](https://doi.org/10.48550/arXiv.1703.04977)

Launhardt, R., Pavlyuchenkov, Y., Gueth, F., et al. 2009, *A&A*, 494, 147, doi: [10.1051/0004-6361:200810835](https://doi.org/10.1051/0004-6361:200810835)

Launhardt, R., Pavlyuchenkov, Y. N., Akimkin, V. V., et al. 2023, *A&A*, 678, A135, doi: [10.1051/0004-6361/202347483](https://doi.org/10.1051/0004-6361/202347483)

Lynden-Bell, D. 1996, *MNRAS*, 279, 389, doi: [10.1093/mnras/279.2.389](https://doi.org/10.1093/mnras/279.2.389)

Mattia, G., & Fendt, C. 2020, *ApJ*, 900, 59, doi: [10.3847/1538-4357/aba9d7](https://doi.org/10.3847/1538-4357/aba9d7)

McKee, C. F., & Tan, J. C. 2002, *Nature*, 416, 59, doi: [10.1038/416059a](https://doi.org/10.1038/416059a)

McKee, C. F., & Tan, J. C. 2003, *ApJ*, 585, 850, doi: [10.1086/346149](https://doi.org/10.1086/346149)

Ouyed, R., Clarke, D. A., & Pudritz, R. E. 2003, *ApJ*, 582, 292, doi: [10.1086/344507](https://doi.org/10.1086/344507)

Pudritz, R. E., & Norman, C. A. 1983, *ApJ*, 274, 677, doi: [10.1086/161481](https://doi.org/10.1086/161481)

Rosen, A. L. 2022, *ApJ*, 941, 202, doi: [10.3847/1538-4357/ac9f3d](https://doi.org/10.3847/1538-4357/ac9f3d)

Sánchez-Monge, Á., Cesaroni, R., Beltrán, M. T., et al. 2013, *A&A*, 552, L10, doi: [10.1051/0004-6361/201321134](https://doi.org/10.1051/0004-6361/201321134)

Shepherd, D. S., & Churchwell, E. 1996, *ApJ*, 472, 225, doi: [10.1086/178057](https://doi.org/10.1086/178057)

Shu, F., Najita, J., Ostriker, E., et al. 1994, *ApJ*, 429, 781, doi: [10.1086/174363](https://doi.org/10.1086/174363)

Staff, J. E., Tanaka, K. E. I., Ramsey, J. P., Zhang, Y., & Tan, J. C. 2023, *ApJ*, 947, 40, doi: [10.3847/1538-4357/acbd47](https://doi.org/10.3847/1538-4357/acbd47)

Staff, J. E., Tanaka, K. E. I., & Tan, J. C. 2019, *ApJ*, 882, 123, doi: [10.3847/1538-4357/ab36b3](https://doi.org/10.3847/1538-4357/ab36b3)

Sun, R., Jia, P., Sun, Y., et al. 2023, *AJ*, 166, 235, doi: [10.3847/1538-3881/ad01b5](https://doi.org/10.3847/1538-3881/ad01b5)

Tan, J. C., Beltrán, M. T., Caselli, P., et al. 2014, in *Protostars and Planets VI*, ed. H. Beuther, R. S. Klessen, C. P. Dullemond, & T. Henning, 149–172, doi: [10.2458/azu_uapress_9780816531240-ch007](https://doi.org/10.2458/azu_uapress_9780816531240-ch007)

Vasudev, V., Rajesh, M. V., Sreekumar, G., & Shemi, P. M. 2025, *Ap&SS*, 370, 65, doi: [10.1007/s10509-025-04455-2](https://doi.org/10.1007/s10509-025-04455-2)

Xu, D., Karcheski, J., Law, C.-Y., et al. 2025, *ApJ*, 980, 52, doi: [10.3847/1538-4357/ada8a0](https://doi.org/10.3847/1538-4357/ada8a0)

Xu, D., Law, C.-Y., & Tan, J. C. 2023a, *ApJ*, 942, 95, doi: [10.3847/1538-4357/aca66c](https://doi.org/10.3847/1538-4357/aca66c)

Xu, D., Offner, S. S. R., Gutermuth, R., et al. 2023b, *ApJ*, 958, 97, doi: [10.3847/1538-4357/acfecd](https://doi.org/10.3847/1538-4357/acfecd)

Xu, D., Offner, S. S. R., Gutermuth, R., & Oort, C. V. 2020a, *ApJ*, 905, 172, doi: [10.3847/1538-4357/abc7bf](https://doi.org/10.3847/1538-4357/abc7bf)

Xu, D., Offner, S. S. R., Gutermuth, R., & Oort, C. V. 2020b, *ApJ*, 890, 64, doi: [10.3847/1538-4357/ab6607](https://doi.org/10.3847/1538-4357/ab6607)

Xu, D., Tan, J. C., Hsu, C.-J., & Zhu, Y. 2023c, *ApJ*, 950, 146, doi: [10.3847/1538-4357/accae5](https://doi.org/10.3847/1538-4357/accae5)

Xu, D., Tan, J. C., Staff, J. E., et al. 2024, *ApJ*, 966, 117, doi: [10.3847/1538-4357/ad3211](https://doi.org/10.3847/1538-4357/ad3211)

Zhang, Y., & Tan, J. C. 2011, *ApJ*, 733, 55, doi: [10.1088/0004-637X/733/1/55](https://doi.org/10.1088/0004-637X/733/1/55)

Zhang, Y., & Tan, J. C. 2018, *ApJ*, 853, 18, doi: [10.3847/1538-4357/aaa24a](https://doi.org/10.3847/1538-4357/aaa24a)

Zhang, Y., Tan, J. C., & Hosokawa, T. 2014, *ApJ*, 788, 166, doi: [10.1088/0004-637X/788/2/166](https://doi.org/10.1088/0004-637X/788/2/166)

Zhang, Y., Tan, J. C., & McKee, C. F. 2013, *ApJ*, 766, 86, doi: [10.1088/0004-637X/766/2/86](https://doi.org/10.1088/0004-637X/766/2/86)

Zhang, Y., Tan, J. C., Sakai, N., et al. 2019a, *ApJ*, 873, 73, doi: [10.3847/1538-4357/ab0553](https://doi.org/10.3847/1538-4357/ab0553)

Zhang, Y., Tanaka, K. E. I., Rosero, V., et al. 2019b, *ApJL*, 886, L4, doi: [10.3847/2041-8213/ab5309](https://doi.org/10.3847/2041-8213/ab5309)

Zhang, Y., Tanaka, K. E. I., Tan, J. C., et al. 2022, *ApJ*, 936, 68, doi: [10.3847/1538-4357/ac847f](https://doi.org/10.3847/1538-4357/ac847f)

APPENDIX

A. COMPARISON OF PERFORMANCE FOR THE FOUR MODELS

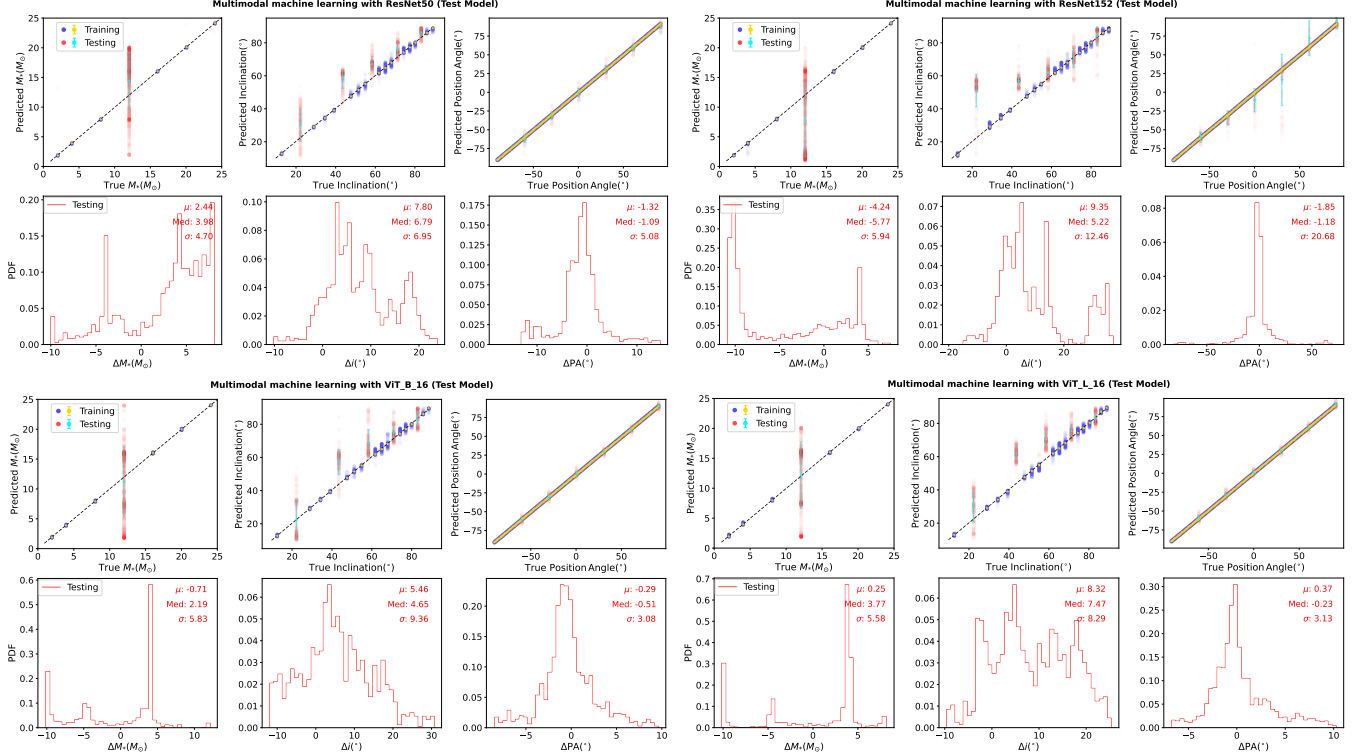


Figure 13. Summary of the performance of four test machine learning models: ResNet50 (upper left), ResNet152 (upper right), ViT_B_16 (lower left), and ViT_L_16 (lower right). These models are trained on a restricted dataset that excludes samples with a protostellar mass of $12 M_{\odot}$ and five specific inclination angles. Model performance is evaluated on outflows corresponding to the excluded mass and inclination angles. In each panel, the top row compares the ground-truth values with the model predictions for protostellar mass, inclination angle, and position angle from left to right. The bottom row shows the probability distribution functions (PDFs) of the prediction errors, defined as the difference between the predicted and true values.

Figures 13–16 compare the performance of ResNet and ViT architectures. We find that ViT models generally offer superior generalization on unseen parameters and greater robustness to spatial resolution degradation (Figure 15). Additionally, ablation studies (Figure 16) confirm that spatial morphology, rather than spectral kinematics, is the dominant driver of the inferred physical parameters, with spectral omission having negligible impact on accuracy for moderate smoothing.

B. GALLERY OF MODEL INTERPRETABILITY VISUALIZATIONS

In this section, we present a comprehensive gallery of interpretability visualizations comparing the decision-making processes of the ResNet50 and ViT_L_16 architectures. We display Smooth Grad-CAM++ attribution maps for predicted outflow mass and the cosine component of the position angle, along with their respective uncertainty estimates, in Figures 17 and 18. Complementing these, we provide pixel-level attribution via Integrated Gradients for the same parameters in Figures 19 and 20. Finally, the results of the Occlusion Sensitivity Analysis are presented in Figures 21 and 22, verifying the causal importance of the identified spatial features.

Collectively, these complementary visualizations confirm that the models drive their inference from physically meaningful spatial structures, such as cavity walls and terminal lobes, providing robust evidence that the learned representations are grounded in the actual physical morphology of the outflows rather than observational artifacts.

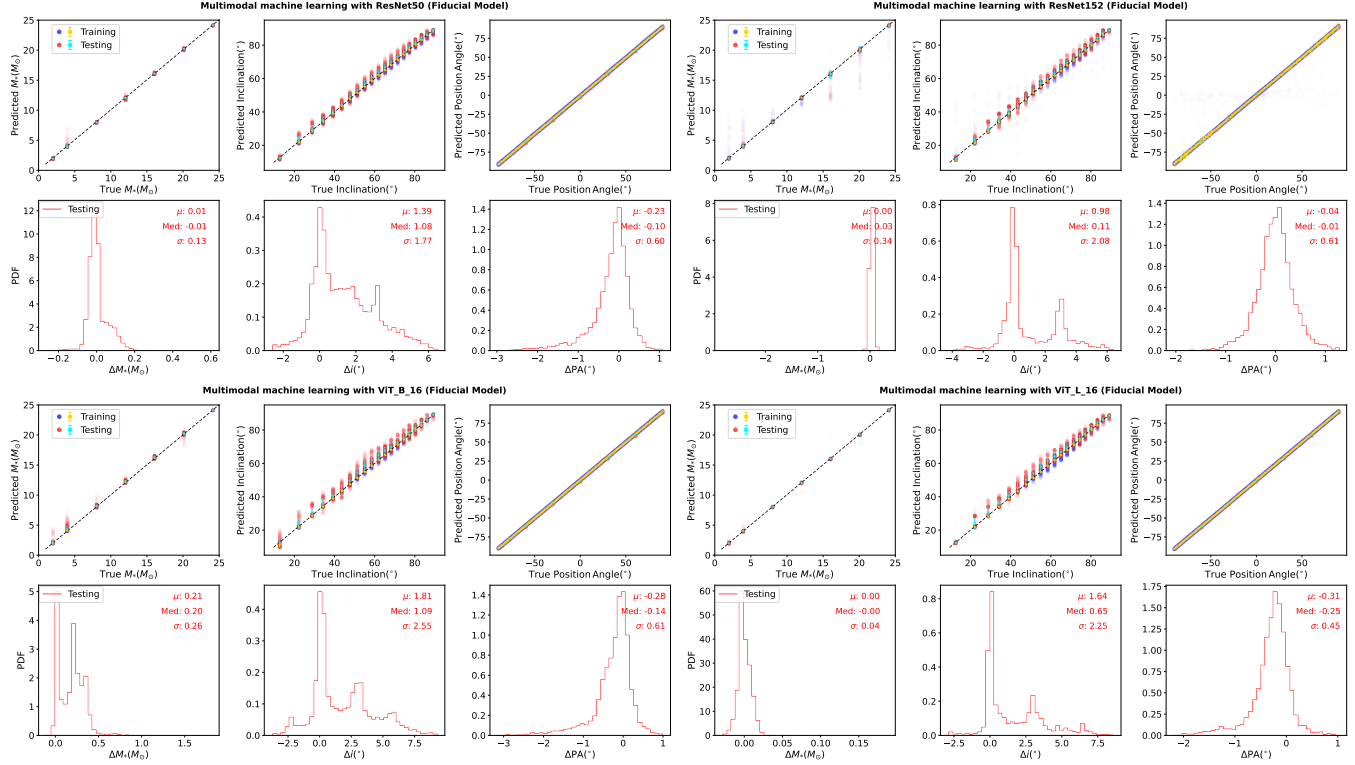


Figure 14. Same as Figure 13, but for models trained on the full range of protostellar masses and inclination angles.

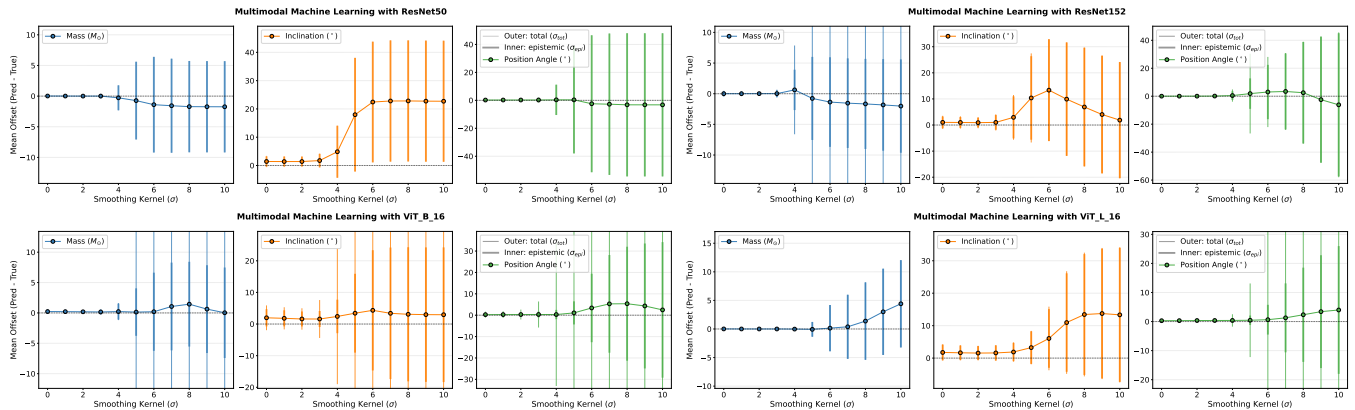


Figure 15. Performance of four machine learning models on synthetic data convolved with progressively larger Gaussian kernels. From left to right, panels show results for protostellar mass, inclination angle, and position angle, including predicted means, total uncertainties, and epistemic (model) uncertainties. The total uncertainty is computed as the quadrature sum of epistemic and aleatoric (data) uncertainties.

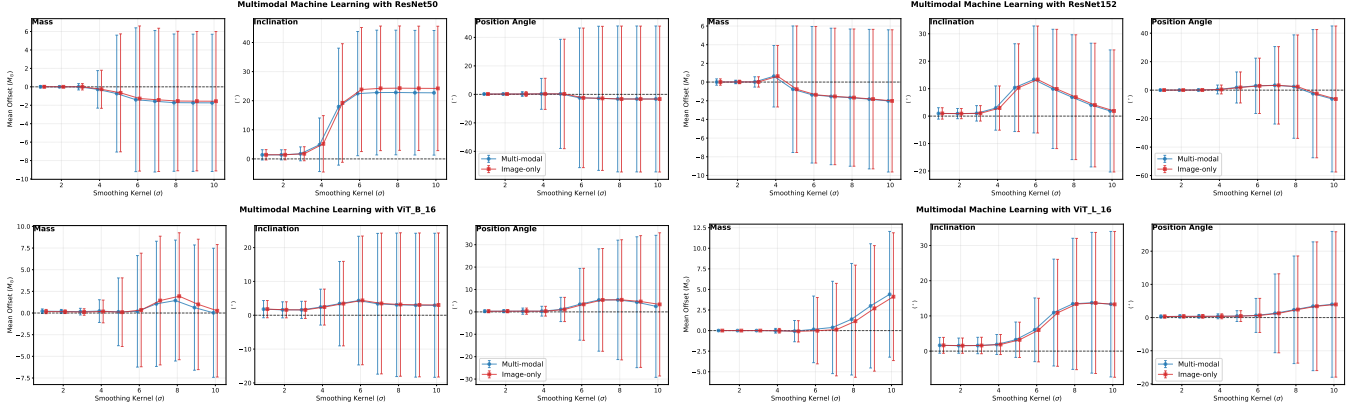


Figure 16. Comparison of model performance for two input configurations: multi-modal (images + spectra) and image-only, evaluated on synthetic data with progressively increased Gaussian smoothing.

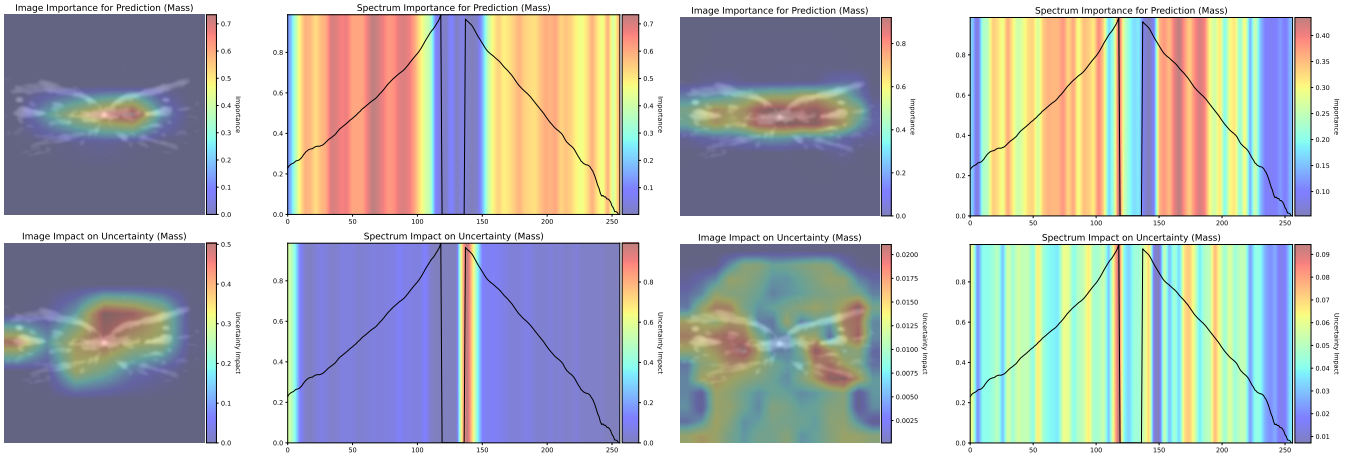


Figure 17. Grad-CAM++ visualizations for outflow mass prediction and its associated uncertainty using the ResNet50 (left panels) and ViT_L16 (right panels) models. In each subplot, the background shows the corresponding test outflow input, image (left) and spectrum (right). The upper row displays the attribution maps for mass prediction, while the lower row shows those for mass uncertainty prediction. The overlaid heatmaps indicate regions that contribute most strongly to the inferred quantities.

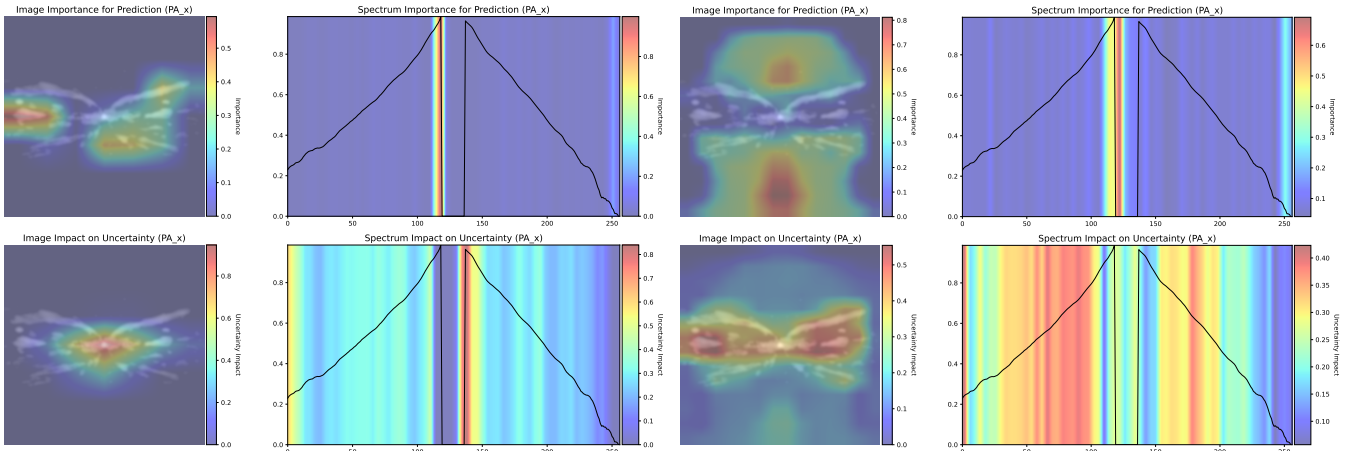


Figure 18. Same as Figure 17, but for Grad-CAM++ visualizations of one component of the position angle (the cosine term) and the corresponding uncertainty prediction.

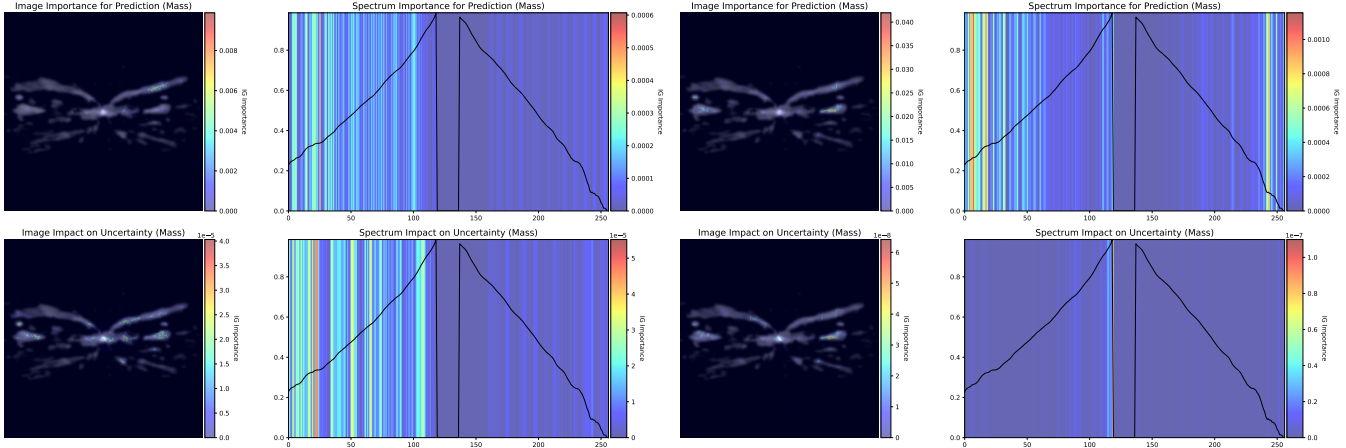


Figure 19. Same as Figure 17, but showing Integrated Gradients maps for the prediction of outflow mass and its associated uncertainty using the ResNet50 (left panels) and ViT_L-16 (right panels) models.

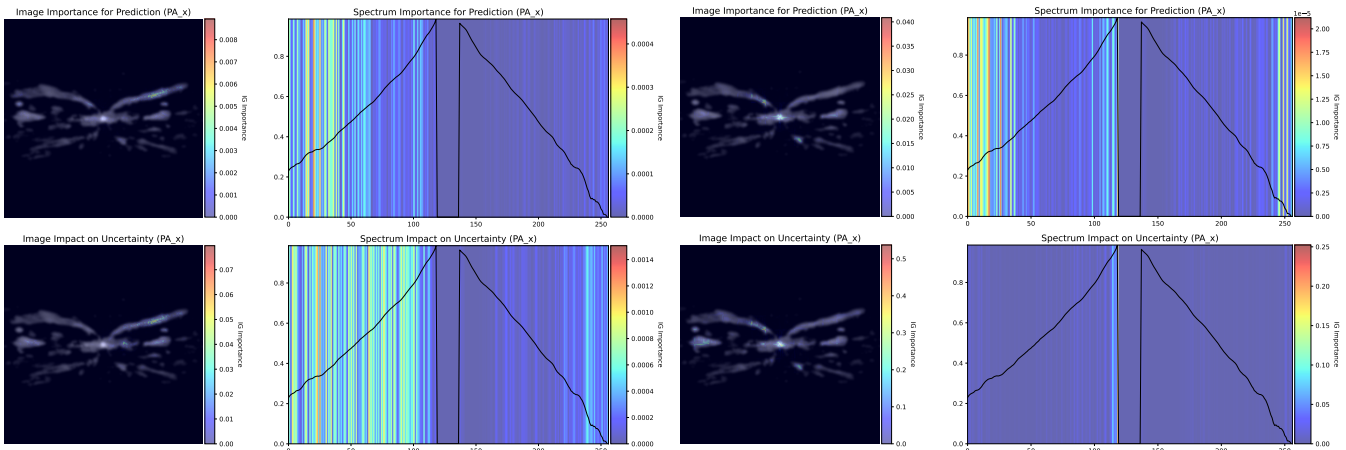


Figure 20. Same as Figure 19, but showing Integrated Gradients maps for one component of the position angle (the cosine term) and its associated uncertainty.

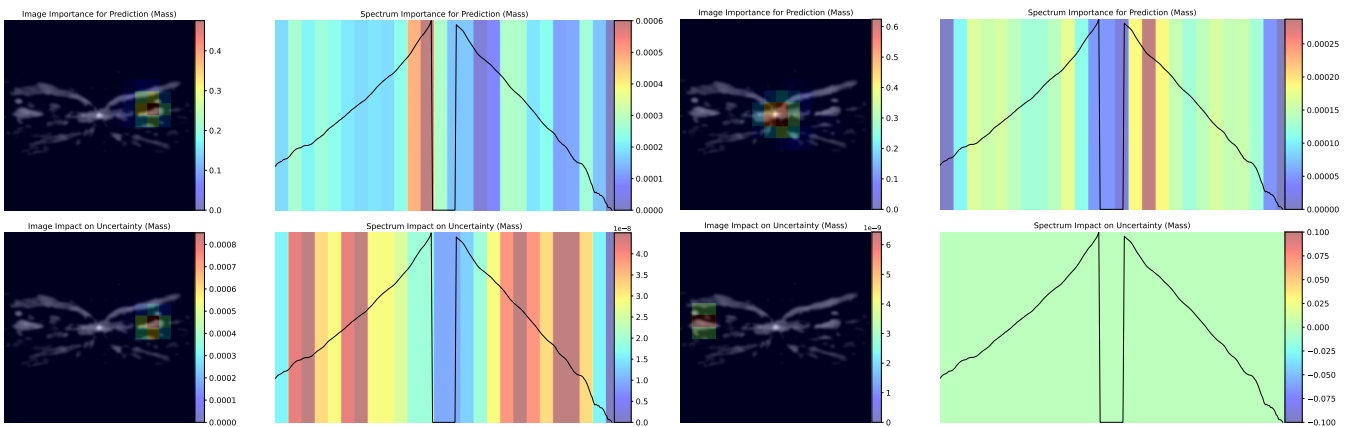


Figure 21. Same as Figure 17, but showing Occlusion Sensitivity Analysis results for outflow mass prediction and its associated uncertainty using the ResNet50 (left panels) and ViT_L-16 (right panels) models.

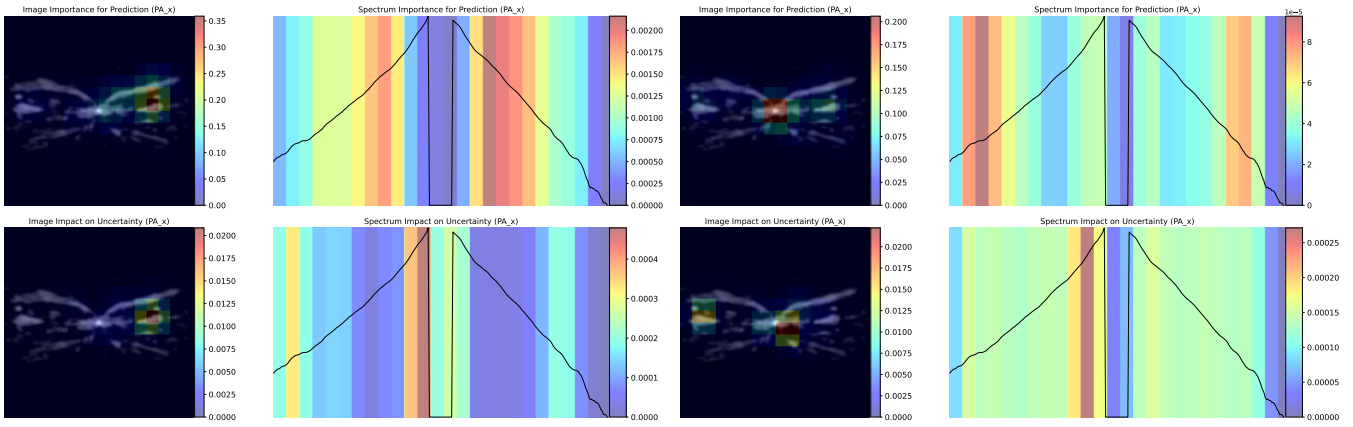


Figure 22. Same as Figure 21, but showing Occlusion Sensitivity Analysis results for one component of the position angle (the cosine term) and its associated uncertainty.